

SPITZER/INFRARED ARRAY CAMERA LIMITS TO PLANETARY COMPANIONS OF FOMALHAUT AND ϵ ERIDANI

MASSIMO MARENGO¹, KARL STAPELFELDT², MICHAEL W. WERNER², JOSEPH L. HORA¹, GIOVANNI G. FAZIO¹,
MICHAEL T. SCHUSTER¹, JOSEPH C. CARSON³, AND S. THOMAS MEGEATH⁴

¹ Harvard-Smithsonian Center for Astrophysics, 60 Garden Street, Cambridge, MA 02138, USA; mmarengo@cfa.harvard.edu

² Jet Propulsion Laboratory, California Institute of Technology, 4800 Oak Grove Drive, Pasadena, CA 91109, USA

³ Max-Planck-Institut für Astronomie, Königstuhl 17, 69117 Heidelberg, Germany

⁴ The University of Toledo, 2801 West Bancroft Street, Toledo, OH 43606, USA

Received 2009 April 10; accepted 2009 June 4; published 2009 July 15

ABSTRACT

Fomalhaut and ϵ Eridani are two young, nearby stars that possess extended debris disks whose structures suggest the presence of perturbing planetary objects. With its high sensitivity and stable point-spread function, *Spitzer*/Infrared Array Camera (IRAC) is uniquely capable of detecting cool, Jupiter-like planetary companions whose peak emission is predicted to occur near $4.5 \mu\text{m}$. We report on deep IRAC imaging of these two stars, taken at 3.6 and $4.5 \mu\text{m}$ using subarray mode and in all four channels in wider-field full array mode. Observations acquired at two different telescope roll angles allowed faint surrounding objects to be separated from the stellar diffraction pattern. No companion candidates were detected at the reported position of Fomalhaut b with 3σ model-dependent mass upper limits of $3M_J$ (for an age of 200 Myr). Around ϵ Eridani, we instead set a limit of 4 and $\lesssim 1M_J$ (1 Gyr model age) at the inner and outer edge of the submillimeter debris ring, respectively. These results are consistent with non-detections in recent near-infrared imaging searches, and set the strongest limits to date on the presence of planets outside ϵ Eridani submillimeter ring.

Key words: infrared: stars – planetary systems – stars: individual (Fomalhaut, ϵ Eridani)

Online-only material: tar file

1. INTRODUCTION

Debris disks are dust clouds in extrasolar planetary systems produced by ongoing collisions between small bodies analogous to asteroids and comets. Their internal structure is of considerable scientific interest, for it can directly betray the presence of planets. Narrow rings, warps, central holes, and azimuthal asymmetries can be related to the likely mass and orbital characteristics of the perturbing object (Liou & Zook 1999; Wyatt et al. 1999). Nearby debris disks are thus ideal targets for deep imaging searches for extrasolar planets.

Fomalhaut (α PsA; IRAS 22549–2953) is a bright A3V star 7.7 pc distant, with an estimated age between 100 and 300 Myr (Barrado y Navascues 1998). An inclined circumstellar dust ring, with an inner and outer edge diameter of 260 and 310 AU, respectively, was first resolved by Holland et al. (1998) at $850 \mu\text{m}$. A modest ring brightness asymmetry seen at $450 \mu\text{m}$ (Holland et al. 2003) becomes increasingly prominent toward shorter wavelengths in *Spitzer Space Telescope* images (Stapelfeldt et al. 2004), consistent with models of an eccentric ring that is warmed at periastron. This model was subsequently confirmed in detail by *Hubble Space Telescope* (HST) scattered light imaging (Kalas et al. 2005). The sharpness of the ring inner edge is consistent with dynamical sculpting by a giant planet orbiting nearby (Quillen 2006), recently detected by Kalas et al. (2008) at optical wavelengths.

ϵ Eridani (IRAS 03305–0937) is a K2V star only 3.2 pc distant, with an estimated age of ~ 850 Myr (Di Folco et al. 2004). A submillimeter dust ring, 220 AU in diameter and projected close to face-on, was discovered by Greaves et al. (1998). Azimuthal clumps seen along the ring have been suggested to be dust trapped in orbital resonances with a giant planet (Ozernoy et al. 2000; Quillen & Thorndike 2002), but

the brightness and location of these clumps have not been reproducible (Schütz et al. 2004; Greaves et al. 2005; Backman et al. 2009). Far-infrared imaging and spectroscopy with *Spitzer* indicate the presence of two interior dust rings, with additional planets suggested to clear the radial gaps in the dust distribution (Backman et al. 2009). The star has been the target of many near-infrared companion searches (Macintosh et al. 2003; Carson et al. 2005; Nakajima et al. 2005; Itoh et al. 2006; Biller et al. 2007; Janson et al. 2007, 2008; Heinze et al. 2008; Kenworthy et al. 2009). Several of these studies focused on detecting the radial velocity planet that orbits about $1''$ from the star (Hatzes et al. 2000), but without success.

Models for the emergent spectra of young giant planets show a prominent emission peak near $4.5 \mu\text{m}$, caused by a gap in CH_4 , H_2O , and NH_3 opacity (Burrows et al. 2004; Fortney et al. 2008). *Spitzer*/Infrared Array Camera (IRAC) is well suited to searching for such objects, which in broad-band photometry will appear bright in channel 2 and much fainter in channel 1 (Patten et al. 2006). Two dwarf companions to two nearby stars were discovered in this way by Luhman et al. (2007). A deep IRAC search for planetary companions to ϵ Eridani was conducted by Marengo et al. (2006). No companion candidates were found to a model-dependent mass limit of 1 Jupiter mass, in the region $r \gtrsim 25''$ (80 AU). Inside this radius, the imaging sensitivity was compromised by bright star artifacts.

The IRAC subarray imaging mode offers rapid readouts and exposure times as short as 0.02 s. To probe the $5''$ – $20''$ region where the Fomalhaut and ϵ Eridani debris rings are found (and where planetary companions perturbing the rings are expected), we conducted a program of deep IRAC subarray imaging of these two stars. In this paper, we present the results of our IRAC subarray imaging search, a new analysis of the wider-field IRAC full array data set, limits to the surface brightness

Table 1
Observing Log

Source	Mode	AOR KEY	Obs. Date [JD-2400000.5]	Tot. Exp. (s)	Wavelengths (μm)
Fomalhaut	Full	4875776	53337.306	499.2	3.6, 4.5, 5.8, 8.0
Fomalhaut	Full	9015040	53309.253	499.2	3.6, 4.5, 5.8, 8.0
Fomalhaut	Subarray	18951936	54063.253	1468.8	3.6, 4.5 ^a
Fomalhaut	Subarray	18952192	54095.207	1468.8	3.6, 4.5
ϵ Eridani	Full	4876032	53013.836	3369.6	3.6, 4.5, 5.8, 8.0
ϵ Eridani	Full	4876288	53052.781	3369.6	3.6, 4.5, 5.8, 8.0
ϵ Eridani	Subarray	18951424	54147.336	1468.8	3.6, 4.5
ϵ Eridani	Subarray	18951680	54356.199	1468.8	3.6, 4.5

Note.

^a Total Exposure time for the 4.5 μm image is 1419.5 s.

of the debris disks at IRAC wavelengths, and limits to the mid-infrared brightness of Fomalhaut b and of planets in proximity of the ϵ Eridani rings.

2. OBSERVATIONS AND DATA REDUCTION

The observations are summarized in Table 1. The IRAC subarray observations were carried out as a part of *Spitzer* General Observer (GO) program 30754 using only band 1 (3.6 μm) and band 2 (4.5 μm). Each observation requested 255 repeated stacks of 64×0.02 s frames (0.01 s integration time) on nine dither positions, spaced over the subarray on a small-scale Reuleaux triangle. The choice of the frame time and dither pattern was guided by the need to reduce saturation as much as possible and provide the best image sampling on the under-sampled IRAC pixel grid, in order to allow the removal of the stellar point-spread function (PSF). Fomalhaut was observed with this sequence on 2006 November 24 and 2006 December 26, with a $11^\circ 67'$ clockwise roll angle offset between the two epochs. ϵ Eridani was observed on 2007 February 16 and 2007 September 13, providing a $169^\circ 03'$ roll angle offset. The total on-source integration time for each sequence of $9 \times 225 \times 64 = 146,880$ frames was 1468.8 s. The first Fomalhaut sequence executed on 2006 November 24, however, was cut short due to a bug in the *Spitzer* time allocation software, skipping the last 77 repeats in the final dither position while observing in band 2. The integration time for the Fomalhaut first epoch 4.5 μm observation is thus only 1419.5 s. The total field of view for the subarray observations is $\sim 44''$.

IRAC full array observations of Fomalhaut took place on 2004 October 31 and 2004 November 28, as a part of Guaranteed Time Observer (GTO) program 90. The roll angle offset between the two epochs was $11^\circ 03'$ clockwise. At each epoch, the observations consisted of four 12 s frames (10.4 s integration time) taken at each of 12 dither positions spaced over the array on a small-scale Reuleaux triangle. The total integration time was 499.2 s in each of the four IRAC bands. The total field of view imaged in each band was $\sim 5'.78$. ϵ Eridani was observed on 2004 January 9 and 2004 February 17 with a roll angle offset of $20^\circ 15'$ clockwise. The total integration was of 3369.6 s in each of the four IRAC bands, obtained using individual 12 s frame time observations on a 36 points Reuleaux small-scale dither pattern, repeated nine times in each position. The ϵ Eridani full frame IRAC data have been previously presented in Marengo et al. (2006). We include here a new analysis of these data to take advantage of the latest photometric calibration of IRAC, and to ensure a consistent data reduction of the full frame images with the subarray observations.

The two stars, in both subarray and full frame observations, are saturated. While the full frame data are saturated within a radius of $\sim 6''$ from the star, the much shorter frame time of the subarray observations restricts saturation to the central 1–2 IRAC pixels ($\sim 1'.5$ – $3''$ radius). This allows us to search for low-mass companions in the subarray data at closer distances from the star than in the full frame data.

2.1. Data Reduction

Basic data reduction for all the observations was performed with the *Spitzer* Space Center (SSC) IRAC Pipeline version S15, which produced Basic Calibrated Data (BCD) frames and data quality masks for each individual full frame and subarray exposure. The full frame data were reduced using the IRACproc package (Schuster et al. 2006), to obtain a single flux calibrated mosaic combining all the individual exposures in each epoch and each band, on a pixel grid with $0'.24$ pixel⁻¹ resolution. IRACproc is based on the SSC mosaic software MOPEX and provides enhanced outlier (cosmic rays) rejection.

We reduced the subarray data with our custom software, due to the very large number of frames acquired for each exposure, and to mitigate strong “muxstripe” artifacts in the BCDs. The muxstripe artifacts appear as a “jailbar” pattern repeating with a four columns cadence, and is triggered in the InSb arrays (bands 1 and 2) by the flux of bright sources unbalancing the four multiplexer readout channels. The striping pattern spans the whole array, but is stronger below the triggering source, where an exponential decay pattern is superimposed with the same four column cadence. The muxstripe is poorly characterized (does not scale linearly with the source brightness) and its strength depends on the Fowler sampling numbers of the exposures. We unexpectedly found that for the brightness of our sources and the chosen frame time the muxstripe artifacts were dominating all other sources of noise (as much as ~ 50 times above the expected readout noise in the final mosaics).

An example of the problem is shown in Figure 1 for a stack of 255×64 co-added (with a basic temporal outlier filter) frames (panel a). The first step we took to characterize the artifacts was to isolate them by subtracting the stellar PSF, which we constructed by combining the subarray observations of 25 bright Cepheid stars obtained as part of the General Observer program 30666. These Cepheids are bright enough to provide a high signal-to-noise ratio (S/N) PSF without being saturated. Observed with frame times of 0.1 and 0.4 s, they still suffer from muxstriping, but at a much lower level than our 0.02 s frames, and without the presence of the exponential decay. The “Cepheid PSF” was aligned with each 255×64 co-added

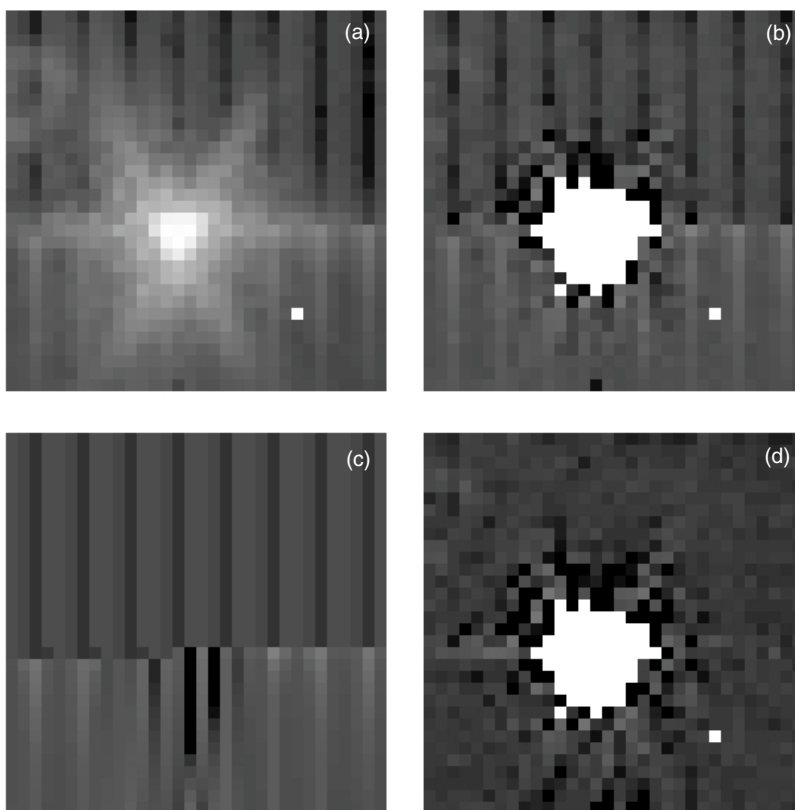


Figure 1. Correction of the muxstripe artifacts for the first dither position of the 2007 February 16 ϵ Eridani observations: (a) co-added stack of 256×64 subarray images; (b) the same stack after PSF subtraction; (c) muxstripe correction matrix; (d) final PSF-subtracted stack with correction applied. The white area at the center of the (b) and (d) panels has been masked to exclude pixels where the muxstripe artifacts cannot be efficiently corrected.

image using the diffraction spikes (typically with a precision of better than $\sim 0''.2$) and subtracted. Figure 1 (panel b) shows the same frame after PSF subtraction. While the PSF structures are not fully removed (due to the different observing parameters and source colors), the muxstriping is more clearly seen. To characterize this artifact, we first equalized the column offset pedestal between the four multiplexer readout channels. We then fitted each column separately, in the lower part of the image, with either an exponential function of the form $y = b \cdot \exp(-x/a) + c$ or a linear slope $y = bx + c$ (in the case of not converging exponential fit). The result of this operation is a “correction matrix” (panel c in Figure 1) that is then applied to the PSF-subtracted 255×64 co-added stack (panel d). The correction was derived independently for each of the nine dither positions, as the artifacts depend on the position of the star on the pixel grid.

The nine individual images obtained for each dither position with the procedure described above were then aligned (using the centroids derived when removing the “Cepheid PSF”) and co-added to produce one image per band, and per epoch, for each source.

2.2. PSF Roll-Subtraction

We have combined the data for the two epochs in one single image for the full frame and subarray observations, separately. By taking advantage of the different roll angle, we have removed the stellar PSF while preserving the other point sources in the field.

In the case of the subarray data, we aligned the two images obtained for each epoch. Even though these images have been already PSF-subtracted with the “Cepheid PSF,” this subtraction

leaves significant residuals because of the different dither pattern adopted. To remove these residuals, we subtracted the aligned images one with the other. After masking in each image the row centered with the subtracted star (where the muxstripe correction is less accurate), we then rotated the subtracted images to have north up and east left. We then averaged them to obtain one single image for each source, in each band (Figure 2). Because of this procedure, point sources in the field of these images would appear as one bright spot sided by two negative sources having half height: inspection of the images in Figure 2 clearly shows that we do not detect any source within the subarray field of view toward either stars.

In the case of the full frame images, we have taken advantage of the availability of a high S/N IRAC PSF to improve the PSF removal beyond what is achievable with the standard two epochs roll-subtraction technique. We derived the full frame IRAC PSF by combining observations of all the stars in the GTO program 90 (two epoch images of ϵ Eridani, Fomalhaut and Vega, one epoch image of ϵ Indi) with the exclusion of β Pic (because of the presence of its debris disk, detected at IRAC wavelengths), plus an image of Sirius obtained as part of the IRAC calibration program. We first reduced the individual PSF star images using IRACproc, producing mosaics on a pixel grid rotated as the IRAC arrays (to preserve the orientation of the PSF features) with a pixel scale of $\sim 0''.24 \text{ pixel}^{-1}$. We masked any pixel with flux higher than 80% of the IRAC saturation limit, to ensure linearity. We then aligned all the images together, using the diffraction spikes as reference (this typically provides an accuracy of $\sim 1/10$ of the pixel grid, or $\sim 0''.02$). Finally, we rescaled all the images to the same reference (one of the images of Vega) and then co-added them together using a median filter

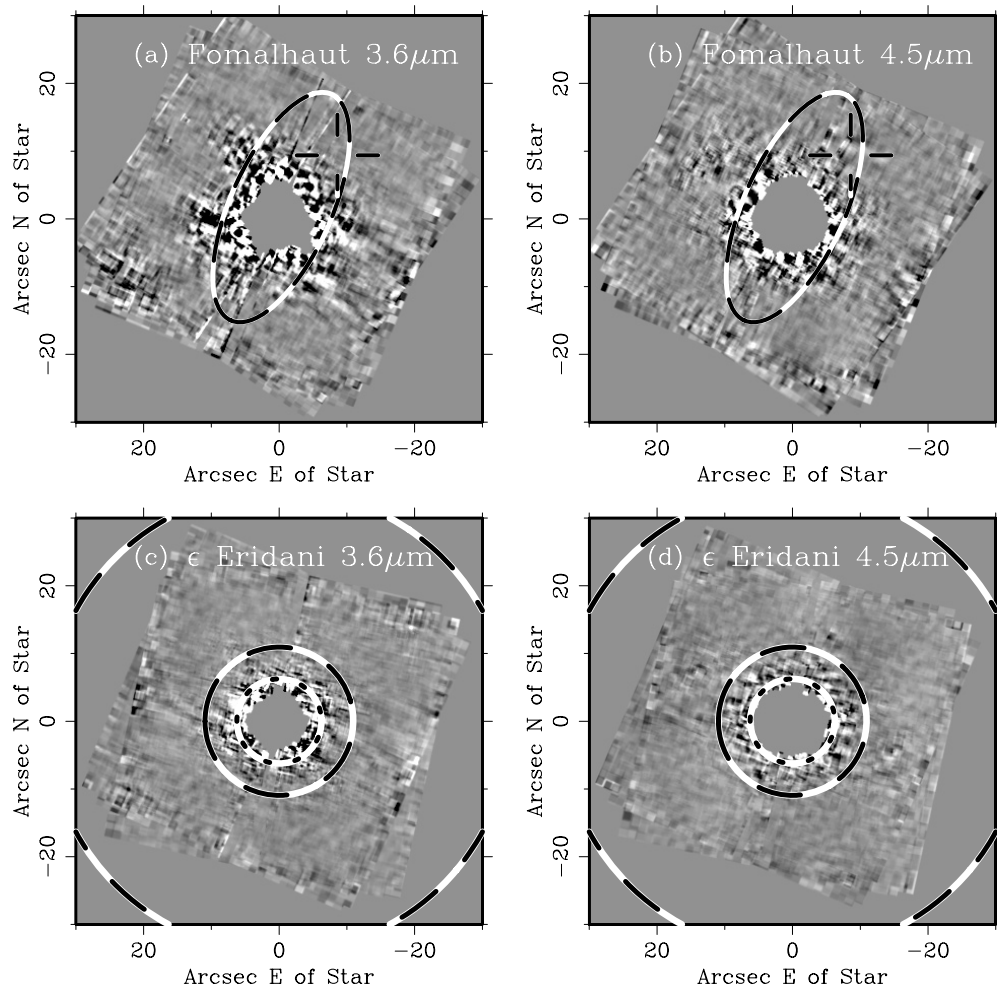


Figure 2. Final roll-subtracted subarray images: (a) Fomalhaut $3.6\ \mu\text{m}$, (b) Fomalhaut $4.5\ \mu\text{m}$, (c) ϵ Eridani $3.6\ \mu\text{m}$, and (d) ϵ Eridani $4.5\ \mu\text{m}$. The images are scaled linearly from -20 to $+20\ \text{MJy sr}^{-1}$. The ellipse and cross in panels (a) and (b) indicate the position of the debris ring and of Fomalhaut b. The dashed circles in panels (c) and (d) indicate the inner and outer radii of the ϵ Eridani submillimeter ring, while the dotted circle shows the location of the $20\ \text{AU}$ “asteroid belt” (from Backman et al. 2009). The central region of each image is masked (because of saturation and PSF-subtraction artifacts). The bright spot NE of ϵ Eridani is most likely a PSF-subtraction artifact, being too narrow (less than $1/2$ of the PSF FWHM) and lacking the two negative aliases expected for real astronomical point sources in the PSF roll-subtracted images.

to reject all point sources in the field. This produced a single PSF image in each band, calibrated to have the same surface brightness (in MJy sr^{-1}) as Vega, cleaned of all point sources in the field. Note that, as a byproduct of this procedure, the normalization factor of the PSF stars are nothing else than the flux ratios of these stars with Vega. These ratios can be expressed as a measure of the Vega magnitudes of the stars, completely independent from the absolute IRAC calibration (because they are the ratios of IRAC images of the stars with an actual image of Vega), and are listed in Table 2. The typical accuracy of these magnitudes is $\sim 0.01\ \text{mag}$. These PSFs are available at the SSC Web site.⁵

The procedure described above is similar to the one adopted in Marengo et al. (2006), but results in a more accurate PSF because of the addition of Sirius and because of a better masking procedure, preserving linearity closer to the center (ensuring more accurate PSF subtractions near the star, which is crucial for this program). While this PSF has a very high S/N and is cleaned of the point sources in the field, it still suffers from uncorrected electronic artifacts (column pull-down, muxbleed, bandwidth effect, and banding). These artifacts are

Table 2
Source PSF-fitting Photometry

Source	[3.6]	[4.5]	[5.8]	[8.0]
Vega ^a	0.00	0.00	0.00	0.00
Fomalhaut	0.98	0.98	0.98	0.98
ϵ Eridani	1.60	1.63	1.61	1.59
ϵ Indi	2.10	2.15	2.12	2.07
Sirius	-1.38	-1.38	-1.38	-1.35

Note.

^a Used as reference, it has 0 Vega-magnitude by definition.

not linearly dependent on the source flux, and are not removed by simple PSF subtraction. To improve this situation, we have derived two specialized versions of the PSF, suitable to remove both electronic and optical PSF features, one optimized for Fomalhaut, and the other for ϵ Eridani.

To achieve this, we first aligned and rescaled the two images of each source (one for each epoch, left in the IRAC array orientation, so that the structures of the PSF will overlap), with the PSF. We then median combined the three-image stack, obtaining a new PSF that (1) in areas free of electronic artifacts,

⁵ <http://ssc.spitzer.caltech.edu/irac/psf.html>

it is the median of the original PSF with the two epoch images; and (2) where electronic artifacts occur, it samples values of the artifacts from one of the two source images. This optimized PSF is free of background sources (which are median filtered) and at the same time has the electronic artifacts scaled appropriately for the source fluency. We then aligned and subtracted the optimized PSF from each of the two epochs, achieving a subtraction of both the optical and electronic structures of the PSF. This subtraction is of higher quality than the standard two epochs roll-subtraction, because the optimized PSFs are free from background sources.

After subtracting each of the two epoch images from their optimized PSF, we projected the result to have north up and east left, and then averaged the rotated images. A sample PSF roll-subtracted image is shown in Figure 3 (bottom panel, the top panel shows the image before PSF subtraction) for Fomalhaut at $4.5 \mu\text{m}$. Figures of the final PSF roll-subtracted full frame images for both sources in all bands are available as a tar file in the electronic version of this paper (Plates 1 to 8).

3. RESULTS

Figures 2 and 3 show that we do not detect any point source at the location of Fomalhaut b indicated by Kalas et al. (2008). We can however use our PSF roll-subtracted subarray and full frame images to set limits on the brightness of the planet in the IRAC bands, and of point sources and extended emission around Fomalhaut and ϵ Eridani.

3.1. Sensitivity

Figures 4 and 5 show the 3σ radial sensitivity for our subarray and full frame images. We estimated the sensitivity curves by measuring the rms noise in circular annuli having a width $dr \simeq 2\text{FWHM}(\lambda)$, where $\text{FWHM}(\lambda)$ is the full width at half-maximum radius of the IRAC PSF in each band. From the rms noise (which is in surface brightness units of MJy sr^{-1}) we have then derived the limiting magnitude in each band, and for each annulus, as follows:

$$m_{\text{lim}} = -2.5 \log \left[\frac{3\pi (\text{FWHM}/2)^2 \cdot \text{rms}}{F_0(r = \text{FWHM}/2)} \right], \quad (1)$$

where F_0 is the flux of the IRAC PSF, normalized as Vega, within a circular aperture with the diameter of the PSF FWHM, and the factor 3 has been introduced to obtain 3σ sensitivities. For a Gaussian noise pattern, these 3σ sensitivities would guarantee a 99.7% detection probability. Given that the PSF-subtraction residual noise is not Gaussian, however, we have tested these sensitivity curves by “planting” point sources of different brightness in the PSF roll-subtracted images, verifying that the plotted 3σ curves indeed guarantee the detection of the sources in all cases.

The two figures also show the expected magnitudes of 1, 2, 5, and $10M_J$ planets of 200 Myr and 1 Gyr of age, interpolated from models by Burrows et al. (2003). Similar estimates can be obtained using the more recent models by Fortney et al. (2008). The vertical line in Figure 4 indicates the projected separation of Fomalhaut b from Kalas et al. (2008), while the vertical lines in Figure 5 show the inner and outer radii of the ϵ Eridani submillimeter ring (from Backman et al. 2009).

The plots show that the subarray images are sensitive to point sources as close as $\sim 3''$ from the central star. The sensitivity at such small radii is generally poor ($\simeq 10$ mag for Fomalhaut and $\simeq 11$ mag for ϵ Eridani), not sufficient to detect planetary

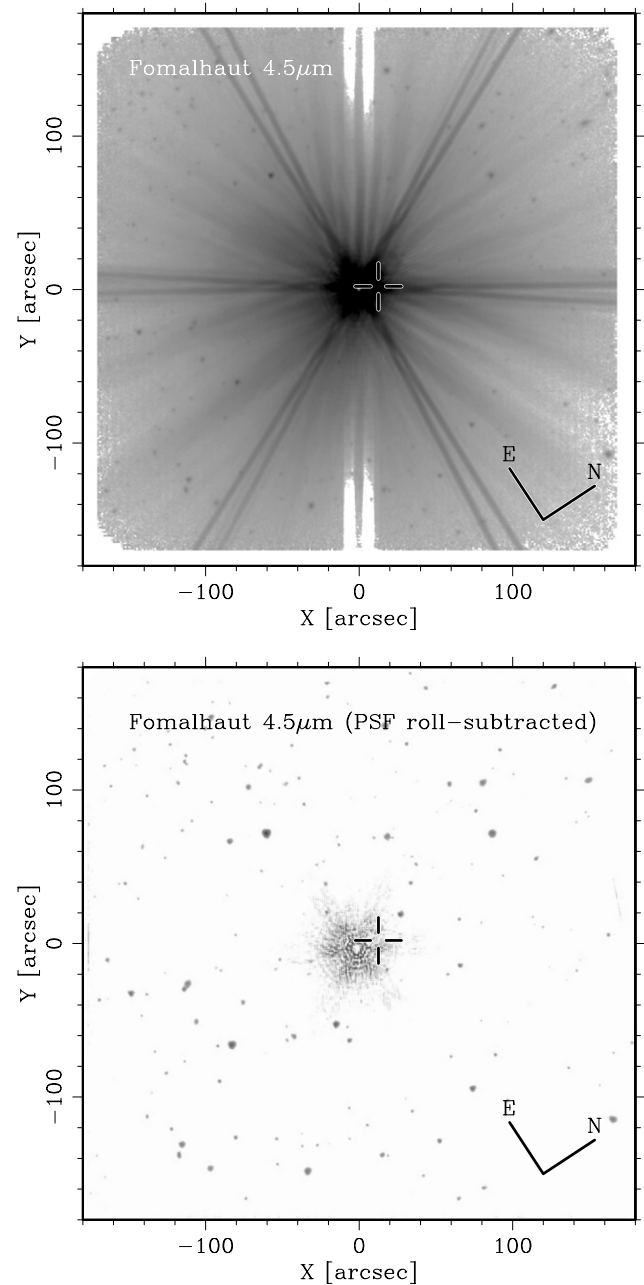


Figure 3. Example of PSF roll-subtraction with IRAC full array data. The top panel shows the Fomalhaut first epoch image ($4.5 \mu\text{m}$). The bottom panel shows the final two-epochs roll-subtracted image of Fomalhaut at the same wavelength. Both images are shown in the logarithmic scale, from 0 to 100 MJy sr^{-1} in the surface brightness color scale. The cross indicates the position of Fomalhaut b. An enlarged figure of the central area around Fomalhaut and ϵ Eridani is shown in Section 3.2.

mass bodies around either stars, but enough to detect T dwarfs. As explained in Section 2, the subarray images sensitivity is limited by the residual errors from the muxstripe correction, and “flattens-out” at radii larger than $15''$. The extent of the muxstripe artifacts in subarray mode was not expected to be so strong at the time these observations were proposed. For radii larger than $\simeq 6''$, however, our new analysis of the full frame PSF roll-subtracted images provides a better sensitivity. Between $\sim 6''$ and $50''$ from the star, our full frame images are limited by the PSF-subtraction noise, while for radii larger than $\sim 50''$ the sensitivity is limited by the noise in the background.

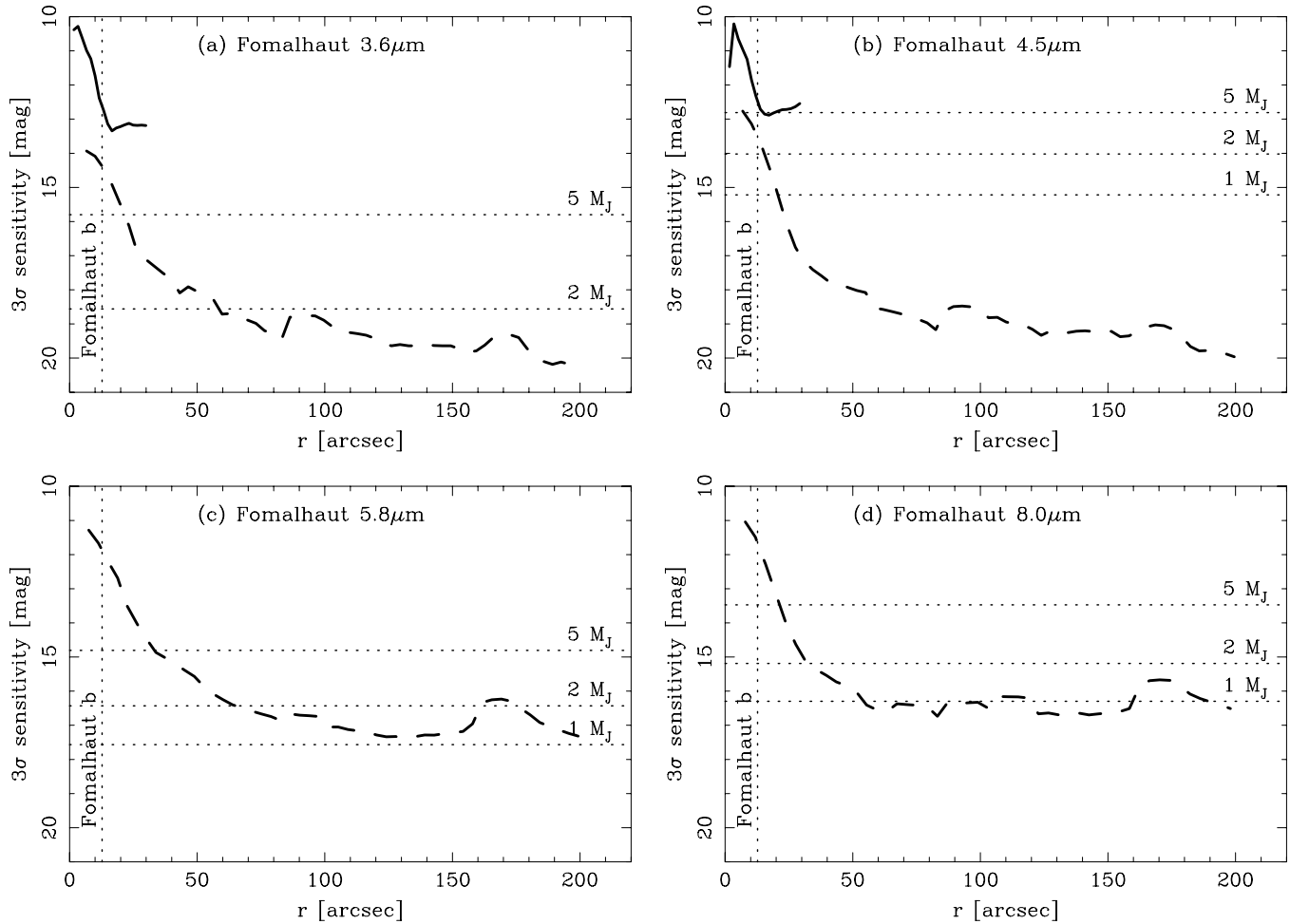


Figure 4. 3σ sensitivity of full frame (dashed lines) and subarray (solid lines) Fomalhaut images: (a) $3.6\ \mu\text{m}$, (b) $4.5\ \mu\text{m}$, (c) $5.8\ \mu\text{m}$, and (d) $8.0\ \mu\text{m}$. The vertical dotted line indicates the projected separation of Fomalhaut b. The horizontal lines indicate the magnitudes of 200 Myr planets interpolated from 100 and 300 Myr models by Burrows et al. (2003). Fortney et al. (2008) models predict a similar $3M_J$ limit at $4.5\ \mu\text{m}$.

Table 3
 3σ Limiting Sensitivity at the Fomalhaut b Radius

Mode	$F_{\text{lim}}(3.6\ \mu\text{m})$ (mJy)	$F_{\text{lim}}(4.5\ \mu\text{m})$ (mJy)	$F_{\text{lim}}(5.8\ \mu\text{m})$ (mJy)	$F_{\text{lim}}(8.0\ \mu\text{m})$ (mJy)
Full frame	0.50	0.70	2.05	1.39
Subarray	2.54	1.83

The 3σ sensitivity limits at the position of Fomalhaut b (Figure 4) show that the planet has a brightness lower than 0.5, 0.7, 2.05, and 1.39 mJy at 3.6, 4.5, 5.8, and $8.0\ \mu\text{m}$, respectively (see Table 3). According to Fortney et al. (2008) this implies a model-dependent mass of $\lesssim 3M_J$ (for a ~ 200 Myr age), in agreement with a similar limit inferred by Kalas et al. (2008) from ground-based near-IR data using the same models. Our images provide the first brightness upper limits for the planet at 4.5, 5.8, and $8.0\ \mu\text{m}$ (an L' band limit is given in Kalas et al. 2008).

From the noise rms derived above, we can also set limits to the surface brightness of the debris disks around both stars, listed in Table 4. Note how our sensitivity at the location of the Fomalhaut ring NW ansa is as much as five times better (1.7 mag) than the sensitivity at the location of the SE ansa. This is because the SE ansa happens to overlap with high noise residuals from PSF “pull-down” electronic artifacts, locally decreasing our sensitivity below the circular average level plotted in Figure 4. Table 4 also shows our sensitivity limits for the ϵ Eridani second

asteroid belt (at 20 AU radius) and for the inner and outer edge of the submillimeter ring (at 35 and 100 AU, respectively) described by Backman et al. (2009).

Macintosh et al. (2003) and Janson et al. (2008) derive limits for the mass of planetary mass bodies inside the inner rim of the ϵ Eridani submillimeter ring of 5 and $3M_J$, respectively, compared to our limit $M \gtrsim 4M_J$ (mass limits estimated for ~ 1 Gyr models). Outside the submillimeter ring, our limit ($M \gtrsim 1M_J$, 1 Gyr model age) is superior to any other available observation, including our previous analysis in Marengo et al. (2006).⁶

3.2. Point Source Photometry

To search for low-mass companions around Fomalhaut and ϵ Eridani, we have measured the photometry of all point sources detected in the PSF roll-subtracted images of both stars. As shown in Figures 4 and 5, we are sensitive to substellar objects with mass lower than $1M_J$ outside the debris rings of both stars (from models with age of 200 Myr and 1 Gyr, respectively).

To measure the photometry of all the point sources in the field of view of the full frame images of both stars, we first converted the data from units of surface brightness flux density

⁶ Note that Figure 7 in Marengo et al. (2006) shows the sensitivity in an area of the PSF-subtracted image far from diffraction spikes or other artifacts. Figure 5 in the present work shows instead a circularly averaged sensitivity, and is superior to the equivalent measure performed on our 2006 PSF-subtracted images.

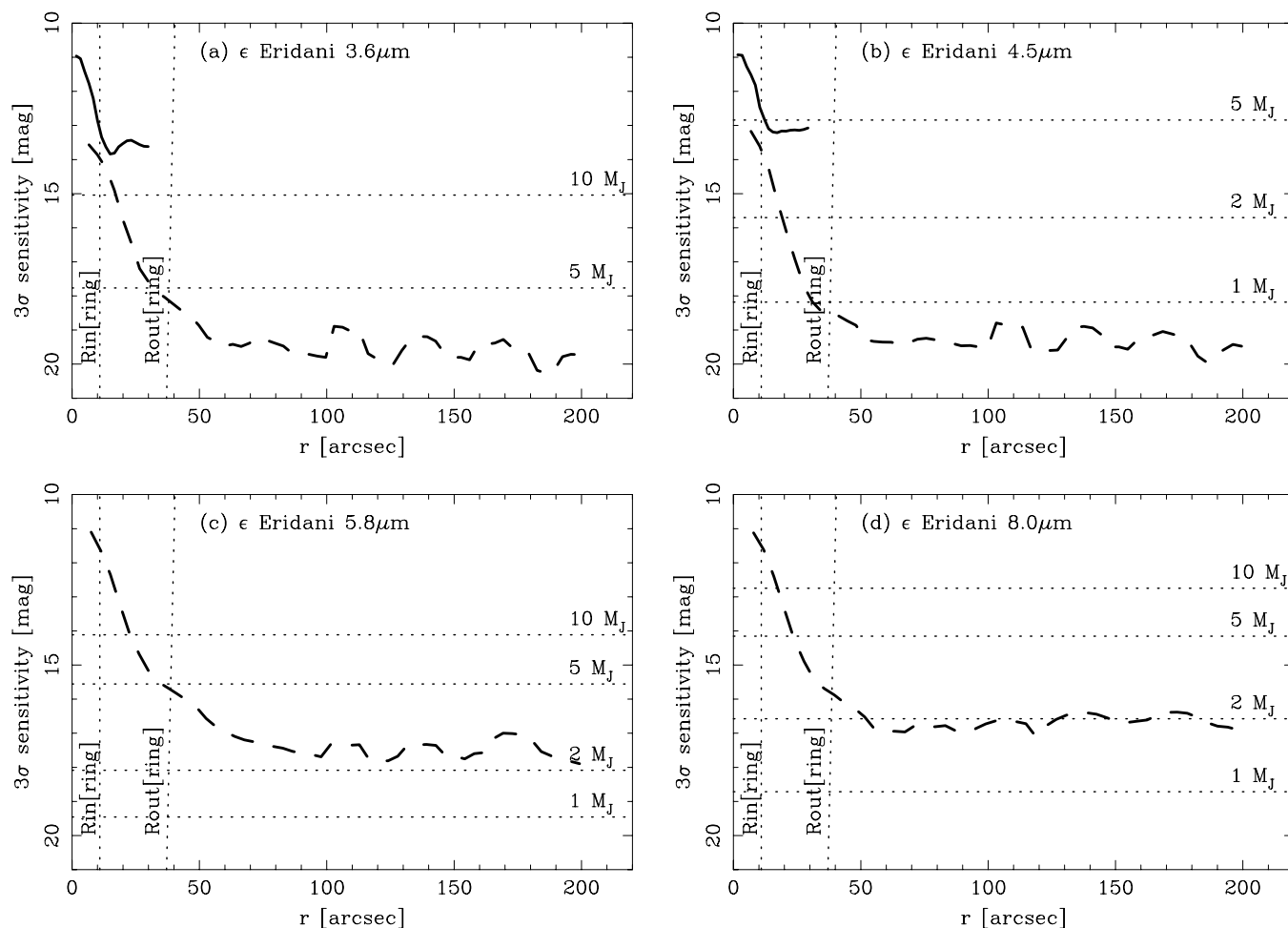


Figure 5. 3σ sensitivity of full frame (dashed lines) and subarray (solid lines) ϵ Eridani images: (a) $3.6\ \mu\text{m}$, (b) $4.5\ \mu\text{m}$, (c) $5.8\ \mu\text{m}$, and (d) $8.0\ \mu\text{m}$. The vertical dotted lines indicate the inner and outer radii of the submillimeter ring, and the horizontal lines the magnitudes of 1 Gyr planet models by Burrows et al. (2003).

Table 4
Fomalhaut and ϵ Eridani Disks Brightness Limits

Mode	$S_{\text{lim}}(3.6\ \mu\text{m})$ (MJy sr $^{-1}$)	$S_{\text{lim}}(4.5\ \mu\text{m})$ (MJy sr $^{-1}$)	$S_{\text{lim}}(5.8\ \mu\text{m})$ (MJy sr $^{-1}$)	$S_{\text{lim}}(8.0\ \mu\text{m})$ (MJy sr $^{-1}$)
Fomalhaut ring (NW ansa)	1.19	1.43	3.84	2.10
Fomalhaut ring (SE ansa)	5.18	5.94	20.26	3.39
ϵ Eridani Asteroid belt 2	2.25	2.07	6.98	2.72
ϵ Eridani submillimeter ring inner edge	1.52	1.20	3.96	1.69
ϵ Eridani submillimeter ring outer edge	0.04	0.02	0.11	0.04

to magnitudes, by dividing by the flux conversion factors found in the image headers of the BCD, and by multiplying by the effective integration time. The IRAC absolute calibration is based on observations of standard stars measured with aperture photometry using a source aperture with a radius of 10 native IRAC pixels ($\sim 12''.2$) in each channel (this is equivalent to state that the aperture correction of 10 IRAC pixel radius apertures is exactly 1 according to this convention). The background was estimated using an annulus centered on the source position with an inner radius and width of 10 IRAC native pixels (Reach et al. 2005). Because our two targets are located in semicrowded fields, we chose to use a smaller source aperture with a radius of $3''.6$ in order to avoid contaminating flux from other, nearby sources. An additional benefit of using a smaller source aperture is an improved S/N for many of the fainter sources. For the background estimation, we used the annulus with an inner radius

of $4''.8$ and a width of $2''.4$. Photometry was extracted using the IRAF phot package. We determined an aperture correction for these nonstandard aperture sizes by comparing the photometry from a set of bright stars in our images using the nominal parameters. We then determined the necessary zero points to produce photometry in the standard calibration defined by Reach et al. (2005). The zero points used are listed in Table 5.

We have first analyzed the colors of all sources detected in multiple IRAC bands. Given the lower sensitivity at 5.8 and $8.0\ \mu\text{m}$, and the CH_4 absorption expected at $3.6\ \mu\text{m}$ for T-dwarfs and gas giant planets, this limits our discovery space to objects with a 200 Myr model dependent mass of $\sim 2M_J$ around Fomalhaut, and $\sim 4M_J$ around ϵ Eridani (1 Gyr model age). We used the same k -Nearest Neighbor method search technique based on the colors and absolute magnitudes of brown dwarf and planet models we adopted in Marengo et al. (2006), described

Table 5
IRAC Photometric Calibration^a

Item	IRAC Band			
	3.6 μm	4.5 μm	5.8 μm	8.0 μm
Isophotal λ (μm)	3.550	4.493	5.731	7.872
FLUXCONV ((MJy sr ⁻¹)/(DN s ⁻¹))	0.1088	0.1388	0.5952	0.2021
GAIN (e DN ⁻¹)	3.3	3.71	3.8	3.8
Zero point magnitudes ^b	16.981	16.512	16.013	15.439
F_V (Vega) (Jy)	280.9	179.7	115.0	64.1

Notes.

^a Based on the IRAC Data Handbook ver. 3.0 (2006).

^b For pixel size 0".24 pixel⁻¹, include aperture correction for 3"6 aperture and sky annulus with 4"8 and 7"2 inner and outer radii.

Table 6
Fomalhaut 3.6 μm Dropout Sources

R.A. [2000]	Decl. [2000]	D (AU)	[4.5]	[5.8]	[8.0]	Notes
344.391700	-29.672331	1391	19.17 \pm 0.17	
344.441542	-29.660608	1074	17.83 \pm 0.04	
344.441542	-29.660608	1074	17.83 \pm 0.04	
344.372933	-29.645378	683	17.96 \pm 0.04	
344.413842	-29.646267	662	18.27 \pm 0.06	
344.399342	-29.641753	543	19.54 \pm 0.00	
344.424521	-29.646136	662	18.52 \pm 0.15	
344.382887	-29.636044	421	18.43 \pm 0.00	
344.424175	-29.644953	629	17.29 \pm 0.05	
344.383133	-29.629925	278	17.59 \pm 0.00	
344.419842	-29.635978	379	17.18 \pm 0.07	...	17.93 \pm 0.45	
344.427429	-29.619778	113	16.05 \pm 0.00	14.70 \pm 0.04	14.81 \pm 0.02	(1)
344.479287	-29.629350	449	17.59 \pm 0.02	
344.433550	-29.617836	177	18.98 \pm 0.00	
344.400317	-29.607925	407	17.54 \pm 0.07	
344.435804	-29.613942	272	17.80 \pm 0.00	
344.416708	-29.609828	348	18.87 \pm 0.00	
344.421133	-29.604700	492	17.12 \pm 0.04	...	15.69 \pm 0.04	(1)
344.419792	-29.600181	616	17.89 \pm 0.05	
344.418371	-29.601414	581	18.52 \pm 0.08	
344.413029	-29.574408	1329	18.22 \pm 0.05	...	17.25 \pm 0.21	(1)
344.423208	-29.568053	1506	17.86 \pm 0.04	...	16.22 \pm 0.06	(1)

Note.

⁽¹⁾ [4.5]–[5.8] or [4.5]–[8.0] color suggest source being a background giant.

in detail in Marengo & Sanchez (2009). None of the sources detected in all four bands of full array imaging had the colors and absolute magnitudes expected for substellar mass objects.

All sources that were detected at 3.6 and 4.5 μm , but missed at 5.8 and/or 8.0 μm , have also been rejected. Based on Burrows et al. (2003) and Fortney et al. (2008) models, none of them possess a [3.6]–[4.5] color red enough to be a planetary mass object for their measured 4.5 μm magnitude.

We then focused on sources detected at 4.5 μm but not detected at 3.6 μm : these sources can be either very red extragalactic sources (Huang et al. 2004; Barmby et al. 2004) or methane dwarfs and planets. Red, mass-losing background giants (such as asymptotic giant branch stars) have positive [4.5]–[8.0] colors (Marengo et al. 2008), and are thus distinguishable from T dwarfs and planets that have instead an 8.0 μm flux equal or lower than the 4.5 μm flux. Tables 6 and 7 list all 3.6 μm “dropout” sources for Fomalhaut and ϵ Eridani, respectively. Note how several of them can be discarded because their flux at 5.8 and 8.0 μm makes them likely to be background mass-losing giants. Comparison with other data sets could enable the rejection of other dropout sources based on (lack of) common proper

motion with the primary star. To our knowledge, however, none of the dropout sources in Tables 6 and 7 has been detected in any other observation at optical or infrared wavelength.

Figure 6 shows the [3.6]–[4.5] versus [4.5] color–magnitude diagram of all sources detected in both IRAC bands 1 and 2 (data points with error bars) and of all 3.6 μm dropout sources (arrows). The [3.6]–[4.5] color of the dropout sources is a lower limit, estimated using the local 3.6 μm 3σ sensitivity derived in Section 3.1. The dropout sources within the Fomalhaut field of view have 4.5 μm magnitudes expected for $\lesssim 1M_J$ 200 Gyr planets, according to Burrows et al. (2003) models. However, their [3.6]–[4.5] colors are still compatible with the colors of red extragalactic sources (e.g., see Stern et al. 2007). Similarly, the dropout sources in the ϵ Eridani field (that, if they were ~ 1 Gyr planets, would have a mass $\lesssim 2M_J$) also have color limits compatible with being background galaxies.

Figure 7 shows the position of the 3.6 μm dropout sources within $50'' \times 50''$ from Fomalhaut and ϵ Eridani, and their relative position with respect to the debris disks. This area corresponds to $\sim 385 \times 385$ AU at the distance of Fomalhaut, and $\sim 160 \times 160$ AU at the distance of ϵ Eridani. Three dropout

Table 7
 ϵ Eridani 3.6 μm Dropout Sources

R.A. [2000]	Decl. [2000]	D (AU)	[4.5]	[5.8]	[8.0]	Notes
53.200488	-9.512958	724	18.32 \pm 0.02	16.13 \pm 0.01	18.20 \pm 0.13	(1)
53.194846	-9.487653	541	18.71 \pm 0.04	...	16.45 \pm 0.06	(1)
53.210854	-9.514525	690	17.93 \pm 0.01	16.79 \pm 0.01	16.05 \pm 0.00	(1)
53.206725	-9.482892	402	18.55 \pm 0.03	
53.213421	-9.489692	417	18.79 \pm 0.03	
53.218321	-9.494831	448	18.89 \pm 0.04	
53.219821	-9.506739	574	18.00 \pm 0.02	
53.219896	-9.509417	604	18.73 \pm 0.04	15.57 \pm 0.01	16.80 \pm 0.04	(1)
53.193787	-9.440481	479	18.49 \pm 0.03	
53.202425	-9.455889	335	18.64 \pm 0.03	
53.219771	-9.481456	299	18.38 \pm 0.04	(2)
53.223296	-9.488964	366	18.92 \pm 0.05	17.48 \pm 0.06	...	(1,2)
53.213246	-9.447133	245	18.56 \pm 0.04	(2)
53.219871	-9.466025	160	16.35 \pm 0.01	
53.217404	-9.469114	204	17.21 \pm 0.02	...	15.67 \pm 0.03	(1)
53.233725	-9.477178	220	17.55 \pm 0.02	
53.202654	-9.420789	543	18.10 \pm 0.02	
53.209637	-9.429756	413	18.86 \pm 0.04	
53.241296	-9.471792	193	18.39 \pm 0.08	
53.239879	-9.477864	246	18.59 \pm 0.06	
53.209096	-9.416711	543	18.08 \pm 0.02	
53.225883	-9.443644	179	18.63 \pm 0.08	
53.243187	-9.458864	135	16.79 \pm 0.03	16.57 \pm 0.14	15.28 \pm 0.02	(1,3,4)
53.238017	-9.463064	93	17.11 \pm 0.10	16.25 \pm 0.14	16.42 \pm 0.12	(1,4)
53.247821	-9.466464	211	18.07 \pm 0.04	17.99 \pm 0.12	17.09 \pm 0.07	(1)
53.258658	-9.484592	436	18.33 \pm 0.02	(2)
53.250783	-9.458222	222	17.31 \pm 0.02	16.73 \pm 0.04	15.69 \pm 0.02	(1)
53.229712	-9.404978	613	18.64 \pm 0.01	
53.245933	-9.422414	444	18.26 \pm 0.02	
53.256567	-9.436811	379	17.77 \pm 0.02	
53.255775	-9.436803	373	17.62 \pm 0.02	
53.283862	-9.494122	731	18.97 \pm 0.02	15.20 \pm 0.00	...	(1)
53.273888	-9.428683	595	17.83 \pm 0.01	16.35 \pm 0.01	15.87 \pm 0.00	(1)

Notes.

- (¹) [4.5]–[5.8] or [4.5]–[8.0] color suggest source being a background giant.
(²) Source listed in Table 5, Marengo et al. (2006).
(³) Source 11 in Table 3, Marengo et al. (2006).
(⁴) Within field of view, but not detected by Macintosh et al. (2003).

sources are detected within 300–400 AU from the Fomalhaut ring, but none of them is in close proximity, or inside, the debris ring. Of these three sources, one has [4.5]–[5.8] and [4.5]–[8.0] color larger than ~ 1.5 , which is characteristic of background mass-losing giants. The other two sources are companion candidates with mass lower than $1M_J$ (according to 200 Myr Burrows et al. 2003 models). Of the four dropout sources detected near ϵ Eridani, one is inside the submillimeter ring. This source, as well as two of the sources detected within ~ 100 AU from the outer radius of the ϵ Eridani submillimeter ring, is likely a mass-losing giant in the background. The remaining source, ~ 90 AU from the outer rim of the debris disk, is a planet candidate with a mass as low as $2M_J$ (based on 1 Gyr Burrows et al. 2003 models).

Of all the dropout sources listed in Table 7, only five were detected at 4.5 μm in Marengo et al. (2006), due to the lower quality of the PSF subtraction in that work. All the other 3.6 μm dropout sources found in Marengo et al. (2006), Table 5, have been detected above 3σ in our current PSF roll-subtracted images, and have been excluded as planet candidates. Thanks to our better sensitivity at 4.5 μm , we detect three sources that were missed by Macintosh et al. (2003) in their field of view. Of these sources, two are 3.6 μm dropouts (shown in Figure 7,

east of ϵ Eridani). The colors of these sources suggest that they are background stars or galaxies.

4. DISCUSSION AND CONCLUSIONS

The physical origin of the optical light detected by Kalas et al. (2008) from Fomalhaut b is unclear. Fortney et al. (2008) model of the thermal emission from a 400 K object of ~ 1.2 Jupiter radius (corresponding to a $3M_J$ object at age 200 Myr) can reproduce the 0.8 μm flux density observed by *HST*. This model is shown in Figure 8, along with the *Spitzer* mid-infrared upper limits from this study and the photometry from Kalas et al. (2008). As already noted by the latter authors, this model predicts a 1.6 μm brightness ~ 5 times larger than the observed upper limit, and a 0.6 μm flux density orders of magnitude fainter than the observed *HST* detection (even taking into account the observed 0.6 μm variability, possibly related to variable H α emission from a hot planetary chromosphere). Reconciling the thermal emission model to the observations would require an additional physical mechanism to produce the 0.6 μm emission, and that atmosphere models be revised to suppress the expected 1.6 μm emission. The *Spitzer* 4.5 μm upper limit lies on top of this thermal emission

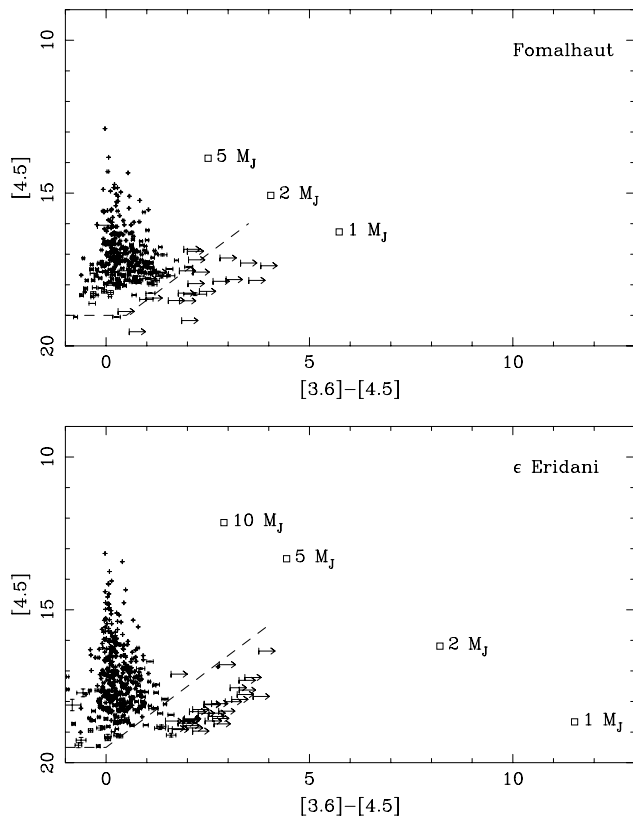


Figure 6. Color–magnitude diagram of all point sources detected in the PSF roll-subtracted $4.5\ \mu\text{m}$ image of Fomalhaut (top) and ϵ Eridani (bottom). Points with error bars are sources detected in both 3.6 and $4.5\ \mu\text{m}$ IRAC bands, while the arrows indicate sources that are undetected at $3.6\ \mu\text{m}$ (for which we used the image sensitivity at the source location as $3.6\ \mu\text{m}$ limit). The squares indicate the colors and magnitudes of planets from Burrows et al. (2003) models, interpolated to the age of each star. The dashed line indicates the average 3σ sensitivity limit of our 3.6 and $4.5\ \mu\text{m}$ images.

model, and thus strengthens these conclusions. Any revision of the thermal emission model to account for the $1.6\ \mu\text{m}$ non-detection *is constrained* by our results. In particular, our $4.5\ \mu\text{m}$ upper limit does not allow a lot of room for the suppressed $1.6\ \mu\text{m}$ luminosity to emerge instead through the largest low-opacity spectral window in methane-dominated atmospheres. The strength of this constraint can only be evaluated through new model atmosphere work directed toward finding a thermal emission solution to the properties of Fomalhaut b. In the interim, reflection from a circumplanetary dust disk remains the simplest model to explain the observed fluxes from the object.

Our surface brightness upper limits (Table 4) for the Fomalhaut ring can be compared to the contrast seen in optical scattered light by Kalas et al. (2008). On the NW ansa, our $3.6\ \mu\text{m}$ limiting surface brightness (in mag arcsec^{-2}) is $17.5\ \text{mag}$ fainter than the star itself. At $0.6\ \mu\text{m}$, the *HST*-detected surface brightness of $21.0\ \text{mag arcsec}^{-2}$ is $19.9\ \text{mag}$ fainter than the star. To escape detection, the $V - L'$ color of the ring must therefore be less than $2.4\ \text{mag}$. $V - L'$ colors of debris disks have however still not been measured, so the strength of our color constraint is unclear. However, the reddest class of Kuiper Belt objects in our solar system has $V - K$ colors less than $1.5\ \text{mag}$ (Cruikshank et al. 2007). If the Fomalhaut dust has similar properties, it thus should not have been detected in our IRAC images.

Similarly, the expected surface brightness of the ϵ Eridani submillimeter ring, as derived by Backman et al. (2009), is at least 1 or 2 orders of magnitude below our sensitivity, in

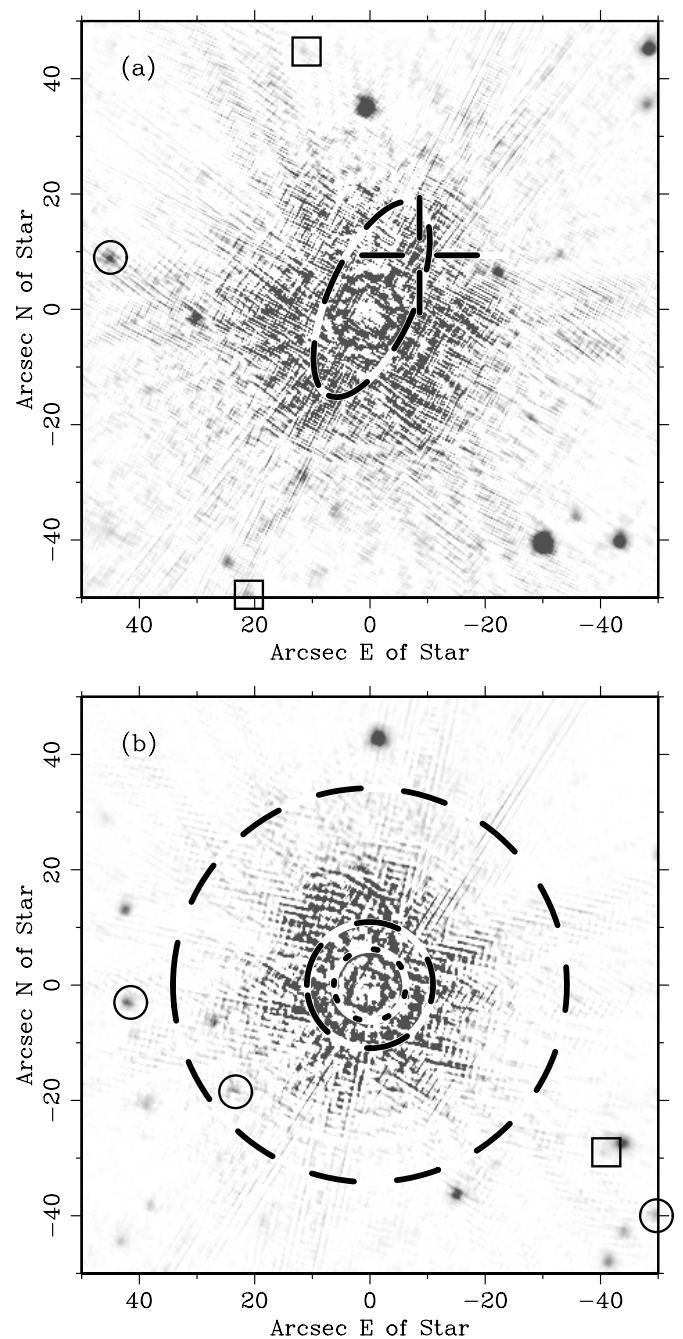


Figure 7. Final $4.5\ \mu\text{m}$ PSF roll-subtracted full frame images. The top panel shows the inner $50'' \times 50''$ ($\sim 385 \times 385\ \text{AU}$) of Fomalhaut. The ellipse indicates the location of the debris ring, and the cross the position of Fomalhaut b. The bottom panel shows the same area (in arcsec, corresponding to $\sim 160 \times 160\ \text{AU}$) around ϵ Eridani. The dotted circle indicates the position of the $20\ \text{AU}$ asteroid belt, while the two dashed circles indicate the inner and outer boundaries of the submillimeter ring as derived by Backman et al. (2009). The images are scaled linearly from 0 to $0.3\ \text{MJy sr}^{-1}$ in the surface brightness color scale. Circle points mark the position of $3.6\ \mu\text{m}$ “dropout” sources that are likely background mass-losing giants, while square points indicate sources detected only at $4.5\ \mu\text{m}$.

agreement with the $0.011\ \text{MJy sr}^{-1}$ Proffitt et al. (2004) limit set by STIS camera observations in scattered light. According to the Backman et al. (2009) model, the ϵ Eridani $20\ \text{AU}$ asteroid belt is expected to have a surface brightness of $\sim 21.7\ \text{mag arcsec}^{-2}$ ($\sim 0.3\ \text{MJy sr}^{-1}$) in the V band, corresponding to $\sim 0.02\ \text{MJy sr}^{-1}$ at $3.6\ \mu\text{m}$. This is also well below the sensitivity limits listed in Table 4 and cannot be detected in our IRAC images.

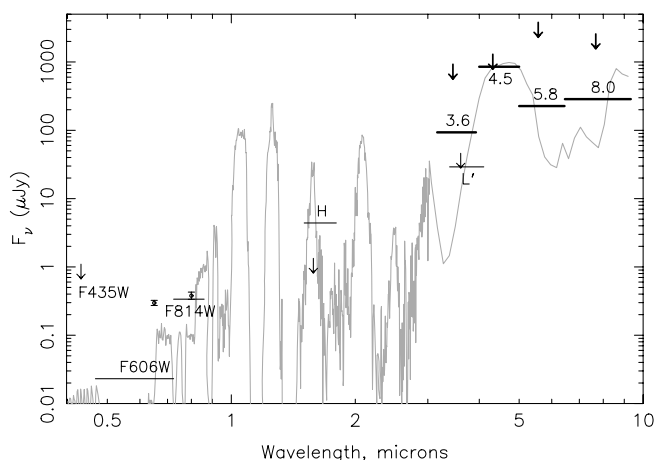


Figure 8. Fomalhaut b spectral energy distribution, compared with the Fortney et al. (2008) model used by Kalas et al. (2008) to fit their data. Optical photometry and 3σ limits are from Kalas et al. (2008). Limits are indicated by the tip of the arrows. IRAC 3σ limits (thick arrows) are from Table 3 in this work. The horizontal bars mark the equivalent broad-band flux found by integrating the model spectrum over the instrumental pass bands. Our $4.5\ \mu\text{m}$ limit, together with the Kalas et al. (2008) near-IR limits, suggest a Fomalhaut b mass lower than $3M_J$ (for a 200 Myr age model), and is inconsistent with the measured optical flux of the planet.

None of the $3.6\ \mu\text{m}$ “dropout” sources listed in Tables 6 and 7 have colors and magnitudes strongly suggesting that they are planetary mass companions of Fomalhaut or ϵ Eridani, rather than red background objects (even though repeated observations aimed to measure common proper motion are required to clarify the issue). Our detection limits for point sources outside the debris disks of Fomalhaut and ϵ Eridani thus imply the likely absence of any widely separated companions of the two stars with mass larger than $1M_J$ (according to Burrows et al. 2003 models of 200 Myr and 1 Gyr age, respectively). Inside the rings (and down to the $3''$ – $6''$ saturation radius of our images) our limits obtained with the *Spitzer* 85 cm aperture telescope are comparable, or superior, to model-dependent mass detection limits from infrared observations obtained at 8–10 m class ground-based telescopes.

We thank John Krist and James Graham for their advice on PSF subtractions and the application of the Fortney atmosphere models to our data set. This work is based on observations made with the *Spitzer Space Telescope*, which is operated by the Jet Propulsion Laboratory, California Institute of Technology, under a contract with NASA. Support for this work was provided by NASA under *Spitzer* General Observer grants 30754 to the Harvard-Smithsonian Center for Astrophysics and to JPL.

REFERENCES

- Backman, D. E., et al. 2009, *ApJ*, **690**, 1522
 Barnby, P., et al. 2004, *ApJS*, **154**, 97
 Barrado y Navascues, D. 1998, *A&A*, **339**, 831
 Biller, B. A., et al. 2007, *ApJS*, **173**, 143
 Burrows, A., Sudarsky, D., & Hubeny, I. 2004, *ApJ*, **609**, 407
 Burrows, A., Sudarsky, D., & Lunine, J. I. 2003, *ApJ*, **596**, 587
 Carson, J. C., Eikenberry, S. S., Brandl, B. R., Wilson, J. C., & Hayward, T. L. 2005, *AJ*, **130**, 1212
 Cruikshank, D. P., Barucci, M. A., Emery, J. P., Fernández, Y. R., Grundy, W. M., Noll, K. S., & Stansberry, J. A. 2007, in *Protostars and Planets V*, ed. B. Reipurth, D. Jewitt, & K. Keil (Tucson, AZ: Univ. Arizona Press), 879
 Di Folco, E., Thévenin, F., Kervella, P., Domiciano de Sousa, A., Coudé du Foresto, V., Ségransan, D., & Morel, P. 2004, *A&A*, **426**, 601
 Fortney, J. J., et al. 2008, *ApJ*, **683**, 1104
 Greaves, J. S., et al. 1998, *ApJ*, **506**, L133
 Greaves, J. S., et al. 2005, *ApJ*, **619**, L187
 Hatzes, A. P., et al. 2000, *ApJ*, **544**, L145
 Heinze, A. N., Hinz, P. M., Kenworthy, M., Miller, D., & Sivanandan, S. 2008, *ApJ*, **688**, 583
 Holland, W. S., et al. 1998, *Nature*, **392**, 788
 Holland, W. S., et al. 2003, *ApJ*, **582**, 1141
 Huang, J.-S., et al. 2004, *ApJS*, **154**, 44
 Itoh, Y., Oasa, Y., & Fukagawa, M. 2006, *ApJ*, **652**, 1729
 Janson, M., Reffert, S., Brandner, W., Henning, T., Lenzen, R., & Hippler, S. 2008, *A&A*, **488**, 771
 Janson, M., et al. 2007, *AJ*, **133**, 2442
 Kalas, P., Graham, J. R., & Clampin, M. 2005, *Nature*, **435**, 1067
 Kalas, P., et al. 2008, *Science*, **322**, 1345
 Kenworthy, M. A., Mamajek, E. E., Hinz, P. M., Meyer, M. R., Heinze, A. N., Miller, D. L., Sivanandan, S., & Freed, M. 2009, *ApJ*, **697**, 1928
 Liou, J.-C., & Zook, H. A. 1999, *AJ*, **118**, 580
 Luhman, K. L., et al. 2007, *ApJ*, **654**, 570
 Macintosh, B. A., Becklin, E. E., Kaisler, D., Konopacky, Q., & Zuckerman, B. 2003, *ApJ*, **594**, 538
 Marengo, M., Megeath, S. T., Fazio, G. G., Stapelfeldt, K. R., Werner, M. W., & Backman, D. E. 2006, *ApJ*, **647**, 1437
 Marengo, M., Reiter, M., & Fazio, G. G. 2008, in *AIP Conf. Proc.* 1001, IXth Torino Workshop on Evolution and Nucleosynthesis in AGB Stars and the IInd Perugia Workshop on Nuclear Astrophysics
 Marengo, M., & Sanchez, M. C. 2009, *AJ*, **138**, 63
 Nakajima, T., et al. 2005, *Astron. Nachr.*, **326**, 952
 Ozernoy, L. M., Gorkavyi, N. N., Mather, J. C., & Taidakova, T. A. 2000, *ApJ*, **537**, 147
 Patten, B. M., et al. 2006, *ApJ*, **651**, 502
 Proffitt, C. R., et al. 2004, *ApJ*, **612**, 481
 Quillen, A. C. 2006, *MNRAS*, **372**, L14
 Quillen, A. C., & Thorndike, S. 2002, *ApJ*, **578**, L149
 Reach, W. T., et al. 2005, *PASP*, **117**, 978
 Schuster, M. T., Marengo, M., & Patten, B. M. 2006, *Proc. SPIE*, **6270**, 627020
 Schütz, O., Nielbock, M., Wolf, S., Henning, T., & Els, S. 2004, *A&A*, **414**, L9
 Stapelfeldt, K. R., et al. 2004, *ApJS*, **154**, 458
 Stern, D., et al. 2007, *ApJ*, **663**, 677
 Wyatt, M. C., Dermott, S. F., Telesco, C. M., Fisher, R. S., Grogan, K., Holmes, E. K., & Piña, R. K. 1999, *ApJ*, **527**, 918